UC Santa Barbara
UC Santa Barbara Previously Published Works

Title

Controlling Operating Voltages in Molybdenum Oxide Anodes through Inductive Effects

Permalink

https://escholarship.org/uc/item/1577v48h

Journal

Chemistry of Materials, 35(13)

ISSN

0897-4756 1520-5002

Authors

Zohar, Arava

Wyckoff, Kira E

Vincent, Rebecca C

et al.

Publication Date

2023-06-26

DOI

10.1021/acs.chemmater.3c00354

Peer reviewed

Controlling Operating Voltages in Molybdenum Oxide Anodes through Inductive Effects

Arava Zohar, Kira E. Wyckoff, Rebecca C. Vincent, Thomas E. Mates, and Ram Seshadri

Materials Department, Materials Research Laboratory, and California NanoSystems Institute, University of California, Santa Barbara, California 93106, United States

Abstract

As Li–ion batteries are more widely adopted, it becomes important to identify new battery electrode materials made from a greater diversity of elements, while improving stability, extracted power, and the ability to charge and discharge rapidly. Early transition metals such as Nb and Mo are relatively earth-abundant elements, with oxides that are candidates for next-generation anode materials. However, Mo oxides are limited as battery electrodes due to their intermediate redox voltages. Lowering this voltage could open the door for high-performance Mo-based oxide anodes. Oxidation of the voltage can be employed by adding redox-inactive cations of electropositive elements. This strategy is named the induction effect and has been proposed as a design principle to raise cathode voltages. However, its use on the anode side appears less common. Here we compare the ionization energy, electrochemistry, and Li diffusivity of the compound $Li_2Mo_4O_{13}$ with MoO_3, which both start out as Mo^{6+} compounds before lithiation. The ionization energy values extracted from ultraviolet photoemission spectroscopy support the hypothesis that the alkali metal cation pushes up the valence band. Electrochemical studies in half-cells against Li/Li^+ indicate that $Li_2Mo_4O_{13}$ can reversibly take up two additional Li in the unit cell. Moreover, the addition of Li to the molybdenum oxide structure lowers the voltage by 300 mV for the $Mo^{6+/5+}$ couple compared to the same redox couple in MoO_3 and retains high Li^+ diffusivity. This work, in conjunction with experimental redox voltages extracted from prior literature on $Ti^{4+/3+}$ and $Nb^{5+/4+}$ redox couples, demonstrates the utility of using inductive effects to tailor the operating voltage of candidate anode materials.

TOC
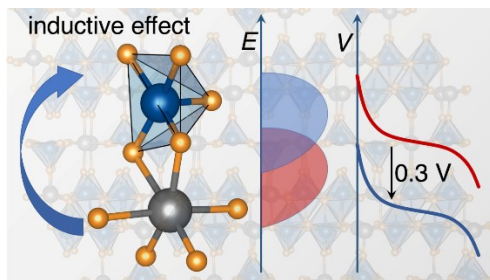
Introduction

The urgent need to develop and deploy renewable energy sources across the world requires constant re-examination of the materials employed for electrochemical energy storage. Current materials used in batteries frequently comprise of scarce and geopolitically sensitive elements such as Co[1], motivating the search for new materials. Battery materials that comprise of earth-abundant elements must retain the advantages of currently used materials, notably appropriate voltages, stable structures across cycling conditions, and networks that permit fast Li diffusion. Furthermore, improvements in rate-performance and the output power can specifically support accelerated adoption of electric vehicles.

The extracted power in a battery is a product of the potential gradient (operating voltage) between two electrodes and capacity (the electrical current normalized to active mass or volume) of the limited electrode. To achieve high power performance, both the potential and the current should be maximized. Here we propose a strategy to increase the operational voltage of a battery by tuning the anode redox voltage. Ideally, the redox voltages of the anode and cathode should be close to the edges of the voltage stability window of the electrolyte. For example, the widely used system $LiPF_6$ in EC:DMC is stable between 0.8 V to 4.4 V.[2] Strategies to modify the cathode voltage have been studied by several groups. For example, Hautier et $al.$[3] have performed a large-scale computational evaluation of phosphate-based compounds to predict battery performance, with an emphasis on the operating voltage of the cathode. Their calculations showed that the redox voltage can vary up to 1 V for various redox-active transition metals, such as V, Mn, Fe, and Co, as a function of the paired anion. Melot et al.[4] experimentally demonstrated induction effects by tuning the voltages across Fe-based cathode materials by more than 1 V by changing the covalency of the metal-oxygen bonds with different anions. However, Gutierrez et $al.$[5] noted that coordination number changes can also affect the voltage, and deconvolution of these affects should be treated with care.

The current commercial cathode material is $LiNi_{0.8}Mn_{0.1}Co_{0.1}O_2$[6], with an operational voltage of 4.2 V, which is optimized to the HOMO of the liquid electrolyte located at 4.5 V. The ideal anode redox voltage would be just above the lower edge of the stability window of the liquid electrolyte, at approximately 1 V $vs.$ Li/Li$^+$. Graphite is the prototypical anode material and has a lithiation potential below 0.5 V $vs.$ Li/Li$^+$.[7,8] This low potential maximizes the full cell voltage, but amplifies safety concerns because low voltages can accelerate the detrimental formation of dendrites and decomposition of the electrolyte. Exploring new anode materials with redox voltages above 1 V would mitigate these concerns. Complex oxides of early transition metals such as Ti, Nb, and Mo tend to have redox couples in this regime. These elements are also relatively stable in multiple oxidation states, which can contribute to higher gravimetric capacities. A combination of edge-sharing and corner-sharing transition metal octahedra provides structural stability along with good ionic and electronic conductivity, qualities necessary for high-rate cycling.

Molybdenum oxides, in particular, are of interest due to their rich chemistry associated with multiple valence states.[9–12] Molybdenum oxide compounds containing Mo^{6+} can be reduced to Mo^{4+}, meaning that each Mo can take two electrons. Recent work by Vincent et $al.$[13] introduces a promising new electrode material, Mo_4O_{11}, that retains an impressive capacity at fast rates (270 mAh g^{-1} at 1C). This work demonstrated the commercial potential of a Mo-based anode, but

highlighted their relatively high redox voltages (about 2 V) as the main disadvantage. This higher anodic voltage leads to a lower full-cell operational voltage, resulting in lower energy and power densities. Because of the aforementioned abundance and high rate capabilities of Mo, there is a motivation to develop strategies to lower the voltage of M0-based anode materials.

Goodenough and coworkers[14] first introduced the induction effect in the context of electrode materials. Their approach was based on the knowledge that the voltage of a transition metal–redox pair is affected by the nature of anions in the structure. Namely, the covalency of the metal–oxygen (M–O) bonds is affected by the electronegativity of the other ions that are present. Less covalent (more polar) M–O bonds will result in a higher probability for localized electrons, which are further energetically from the vacuum level. This principle is understood for oxide compounds containing fluoride or sulfate anions, for example. The opposite should happen for less polar (more covalent) M–O bonds. In this case, more electrons will become delocalized, and therefore their energetic positions will move closer to the vacuum level. This is associated with the presence of electropositive elements in the structure. Experimentally, the ionization energy (IE), which is defined as the energy required to pull core electrons (VBM) to the vacuum level, can be an indicator of the covalency of the bond. By comparing the IE values extracted from ultraviolet photoelectron spectroscopy (UPS) of lithiated and non-lithiated materials, it is possible to probe the inductive effect.[15–17]

To understand the impact of the inductive effect to reduce the anodic voltage in Mo-based oxides, the structure and the electrochemical performance of $Li_2Mo_4O_{13}$ was investigated. This ternary lithium molybdenum oxide has been reported previously,[18–20] but its electrochemistry has not yet been well characterized.[21,22] Here we prepare and characterize this compound using electrochemistry, X-ray diffraction, and UPS. UPS measurements support the hypothesis that the addition of electropositive Li to the structure pushes the Mo d-electrons closer to the vacuum level. Compared to the same redox couple in MoO_3, another fully oxidized Mo compound, electrochemistry measurements show a 300 mV lower $Mo^{6+/5+}$ oxidation voltage. Diffusion coefficient values are found to be between 10^{-12} cm^2 sec^{-1} and 10^{-13} cm^2 sec^{-1}, reminiscent of other fast charging oxide anode materials. These results indicate promise for increasing overall battery power by using the inductive effect as a guiding principle to optimize redox voltages in anode material candidates. *Operando* XRD and *ex-situ* XPS measurements suggest that irreversible structural changes following initial lithiation, resulting in decreased capacity. Careful selection of new anode materials, such as Alkali -TM -O compounds, should continue to be examined since they can improve the battery power output by 10% or more.

Experimental

Material synthesis $Li_2Mo_4O_{13}$ was prepared using a two-step solid-state method according to a previously published procedure.[18] The ammonium molybdate (Fisher Scientific) precursor was

dehydrated by placing powder in an alumina crucible and calcining it for 12 h in a box furnace at 750 °C, then ground in an agate mortar and pestle. Powder X-ray diffraction (XRD) was used to verify the purity of the α-MoO_3. Li_2MoO_4 (Sigma-Aldrich 400904) and MoO_3 in a 1:3 molar ratio were ground together using an agate mortar and pestle. The mixed powder was pressed into a pellet (approximately 300 mg of $Li_2Mo_4O_{13}$) and placed in a cylindrical alumina crucible. The crucible was placed in a closed furnace and heated slowly (2 °C per min) to 475 °C for 12 hr, then ground and pressed into a pellet again. The second calcination step was for 16 h at 490 °C.

Powder X-ray Diffraction To confirm the phase purity of the both MoO_3 and $Li_2Mo_4O_{13}$, powder XRD patterns were collected using a laboratory-source Panalytical Empyrean diffractometer with Cu Kα radiation in Bragg–Brentano geometry. Rietveld analysis was performed using TOPAS Academic v6. Patterns were refined against the previously experimentally determined structures for MoO_3 and $Li_2Mo_4O_{13}$[26]. *Operando* XRD were collected using a custom Swagelok-type cell with a Be window approximately 250 μm thick, allowing X-ray penetration into the cell while cycling. The cell was constructed the same way as described in the following electrochemistry section, with the exception that the slurry was cast onto Celgard 2523 separator instead of Cu foil. A pattern was collected every 20 min during the discharge and charge. $Li_2Mo_4O_{13}$ was cycled versus Li metal using a BioLogic SP-200 potentiostat at a C/15 rate.

Electrochemistry Electrochemistry experiments were performed by casting electrodes made from a 80:10:10 (wt %) ratio of $Li_2Mo_4O_{13}$: conductive carbon (TIMCAL Super P): polyvinylidene fluoride (PVDF). The PVDF was first dissolved in N-methylpyrrolidone and mixed in a FlackTek speed mixer at 2000 rpm for 5 min. The conductive carbon and $Li_2Mo_4O_{13}$ were ground in a mortar and pestle for 10 min and then added to the viscous mixture, forming a slurry. The slurry was mixed in the speed mixer for 10 min and later cast using a 200 μm doctor blade. After 3 h, the cast slurry was dried in a vacuum oven at 80 °C overnight. The electrodes were punched into 10 mm diameter disks with a loading between 2 and 3 mg cm^{-2}. The electrodes were brought into an Ar-filled glovebox (H_2O < 0.1 ppm and O_2 < 0.1 ppm) and assembled into Swagelok cells or Hohsen coin cells for electrochemical testing. A glass fiber separator (Whatman GF/D) was soaked in 1 M $LiPF_6$ in EC/DMC 50/50 v/v (Sigma-Aldrich) electrolyte, and a polished Li foil was used as the counter and reference electrode. Cells were discharged to 1.2 V and charged to 3.4 V using BioLogic potentiostats (VMP1 and VMP3). For the galvanostatic intermittent titration technique (GITT) measurements, the cells were charged at a current density of 0.31 μA cm^{-2} for 1 h, followed by open circuit relaxation for 3 h. The procedure was continued until the voltage of the cells reached a preset value. All measurements were carried out at room temperature.

Ultraviolet Photoelectron Spectroscopy (UPS)/X-ray photoelectron spectroscopy (XPS) To obtain the ionization energy (IE) of MoO_3 and $Li_2Mo_4O_{13}$, photoemission experiments were performed in the Thermo Fisher Escalab Xi$^+$ ultra-high vacuum chamber. The UPS data were acquired from He I (21.22 eV) and He II (40.8 eV) excitation lines at a nominal experimental resolution below 150 meV. The oxidation states on the Mo redox were measured by X-ray photoelectron spectroscopy (XPS) for a pristine material as well as for discharged and charged materials. The *ex situ* samples were loaded onto an air-free sample holder in the glovebox to prevent air exposure that could affect the oxidation state of Mo. The samples were measured using a Thermo

Fisher Escalab Xi⁺ XPS equipped with a monochromated Al anode (E = 1486.7 eV). A cluster gun was used for 20 s to clean the surface and improve count intensity for all samples. The XPS data were compared to the non-etched sample data to verify that there was no contribution from surface charging.

Survey scans were collected at 100 eV pass energy with 50 ms of dwell time; two scans were averaged. *Ex situ* spectra were referenced to adventitious carbon at 284.8 eV. High resolution scans of Li and Mo were collected using a pass energy of 20 eV and a dwell time of 100 ms, averaging 10 scans. CasaXPS was used to fit the data using Shirley backgrounds and GL(50) peak shapes. The fit used appropriate spin–orbit splitting and peak area ratios of the Mo. The d-orbital peaks were area-constrained, as the electrons of a d-orbital split into two peaks, Mo $3d_{5/2}$ and Mo $3d_{3/2}$, in a 3:2 area ratio. Each pair of peaks was also constrained to have the same full width at half maximum. The peak splitting energies determined from the fits were set to 3.13 eV[27].

Scanning electron microscopy (SEM) Images were collected on an Apreo C FEG (ThermoFisher) microscope instrument at an accelerating voltage of 10 kV and 1.6 nA. The powder sample was placed on double sided carbon tape to prevent charging. The SEM images were taken using secondary electron (SE) and InLens detectors.

Raman Spectroscopy Raman spectroscopy measurements were performed using a Horiba Jobin Yvon T64000 open-frame confocal microscope with a triple monochromator and LN2 cooled CCD array detector. Data were collected with a 488 nm laser, 1800 cm⁻¹ grating, and 500 μm slit. The laser intensity was 4 mW for a 2 sec exposure time, and 10 spectra were averaged. A short exposure (2 s) followed by a long exposure (5sec) spectrum were compared for each sample to verify that the sample did not decompose due to beam exposure.

Results and Discussion

Solid-state preparation methods yielded the $Li_2Mo_4O_{13}$ phase with a triclinic structure (P–1 space group) depicted in Figure 1a. A double chain along the *a* axis has edge- and corner-sharing of MoO_6 octahedra. In between, there is a single chain of edge-connected tetrahedra, alternately pointing up and down, that runs along the *c* axis. The two kinds of chains create something close to a layered structure connected through the Li-O bond, giving rise to possible sites that are available for the insertion of Li in between the chains. The compound was measured with powder XRD and compared to an earlier reported structure (JCPDS 70-1709) of $Li_2Mo_4O_{13}$.[18,20] All of the diffraction peaks could be indexed and the Rietveld refinement is displayed in Figure 1b. The diffraction intensities of the <010> plain is slightly underfit, suggesting a preferred orientation to compound. The lattice parameters from the refinement are a = 8.578 Å, b = 11.464 Å, c = 8.222 Å, α = 109.18°, β = 96.12°, and γ = 95.93°. A representative SEM image of the powder is displayed in Figure 1c and shows a plate-like morphology of the particles with lengths up to 100 microns. The preferred orientation found through Rietveld refinement is consistent with the layered nature of the crystal structure and resulting plate-like particles.
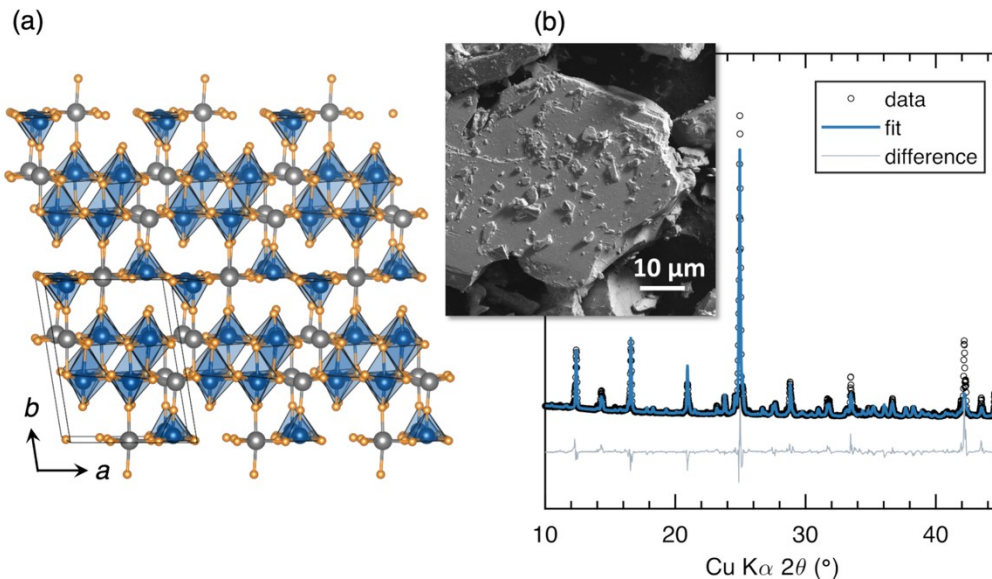
Figure 1. Structural characterization of $Li_2Mo_4O_{13}$. (a) The crystallographic structure of $Li_2Mo_4O_{13}$ projected down the c axis, depicted using VESTA. (b) Powder XRD pattern and Rietveld fit shows a pure phase. The inset displays a representative SEM image of the $Li_2Mo_4O_{13}$ powder after hand-grinding.

The phase diagram of $Li_2Mo_4O_{13}$ indicates that there should be coexistence of a second phase ($Li_4Mo_5O_{17}$ or MoO_3).[19] Therefore, in addition to XRD, Raman spectroscopy (Figure 2) was used to carefully assess the phase purity by investigating the vibrational modes of the lattice. The Raman spectrum of the molybdenum oxide can be divided into three regions:[22–25] (a) the vibration in the range below 400 cm^{-1}, which originates from doubly-coordinated wagging/twisting vibrations of the molybdate groups (b) the intermediate range between 420−745 cm^{-1} which arises mainly from the bending vibrations of Mo−O−Mo bonds, and (c) the higher wavenumber vibrations, 845−1000 cm^{-1}, which arise from the stretching vibrations of the Mo=O bonds.
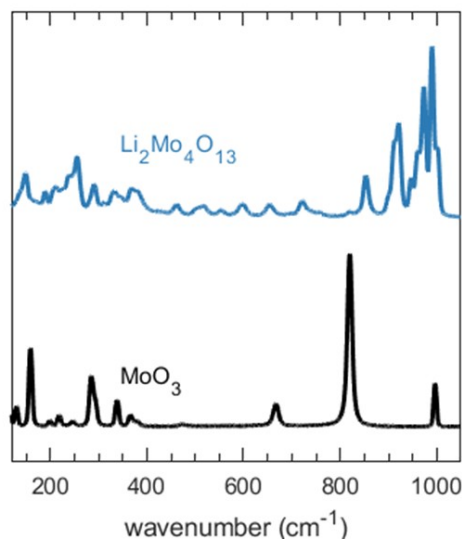
Figure 2. Raman spectra of $Li_2Mo_4O_{13}$ (top) and MoO_3 (bottom) shown for the wavenumber range 120 cm^{-1} to 1050 cm^{-1}. The main Mo=O stretching modes are shifted to higher wavenumber in the lithium-containing compound $Li_2Mo_4O_{13}$, compared to MoO_3.

Figure 2 presents the Raman spectra of $Li_2Mo_4O_{13}$ which shows multiple strong peaks in the high-frequency region from 800 cm^{-1} to 1000 cm^{-1} that correspond to Mo=O stretching modes (1001, 990, 973, 947, 921, 913, 899 and 853 cm^{-1}). The large number of peaks in this regime results from the combination of multiple octahedral coordination environments. The peaks located at 294, 296, 342, 376, 428, and 463 cm^{-1} can be assigned to the translational vibrations of the Li ions. As a reference, the Raman spectra of the layered structure α-MoO_3 (precursor material) was also measured. α-MoO_3 contains one octahedral Mo site which results in 3 main peaks; 996, 820 and 667 cm^{-1}. The 996 cm^{-1} peak is assigned to the stretching modes of Mo=O, the peak at 820 cm^{-1} is assigned to the bridging oxygen vibrations (Mo−O−Mo), and the 667 cm^{-1} peak corresponds to O−Mo−O stretch. For a comparison, the main Raman peaks of the $Li_4Mo_5O_{17}$ phase are expected to be at 153, 212, 278, 812, 868 cm^{-1}, as reported by Khan et al,[26] and are not found in our measured sample. The Raman spectra presented here of $Li_2Mo_4O_{13}$ matches previous measurements and calculations[22], confirming the pure target phase.

Addition of Li to the reduced Mo oxide structure changes the energetic positions of hybridized orbitals between the oxygen and the transition metal atoms, affecting the covalency of the M-O bond. It is not trivial to experimentally measure small changes in the covalency of bonds. The covalency of a bond should be reflected in the energy position of the valence band maximum (VBM), as described in Gutierrez *et al.*[5] and by Greiner *et al.* [27] UPS can measure the energy required to pull an electron to the vacuum level, also known as the ionization energy (IE). The IE of the lithiated and non-lithiated materials were measured with UPS (Figure 3) and plotted with respect to the Fermi level position at 0 eV. Figure 3a displays the full photoemission spectra. Figure 3b shows the cut-off from which the surface work function values was extracted by subtracting the this energy from the He I energy (21.22 eV). Figure 3c displays a zoom-in to the energy regime of the

7

occupied states below the fermi level. The UPS spectra of both materials are similar, although notably, the $Li_2Mo_4O_{13}$ curve (blue diamond) in Figure 3c shows an elevated intensity close to the top of the valence band (10 eV to 4 eV). The IE were found to be 8.7 eV for MoO_3, and 8.6 eV for $Li_2Mo_4O_{13}$. The work function (E_F), defined as the energy from the Fermi level to the vacuum level, was found to be 5.05 eV for both MoO_3 and $Li_2Mo_4O_{13}$. Those results show that the position of the d-orbitals for the lithiated structure $Li_2Mo_4O_{13}$ is roughly 0.1 eV closer to the vacuum level than MoO_3. The lower IE of the lithiated structure aligns with our hypothesis that adding cations to a structure can reduce the energy necessary for a redox reaction because the d-electrons, which participate in the electrochemical reaction, are closer to the vacuum level.
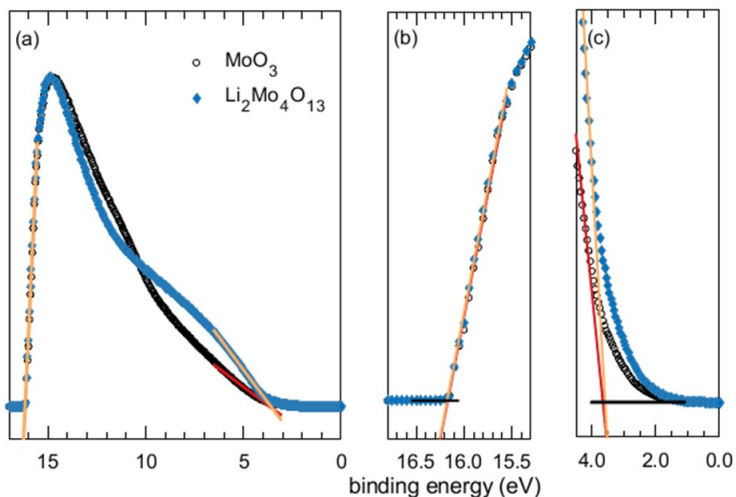

Figure 3. UPS spectra of $Li_2Mo_4O_{13}$ and MoO_3. The left panel (a) shows the raw UPS spectra for both materials with a linear fit. The middle panel (b) displays the photoemission cut-off (intersection of black and orange linear fits) from which the vacuum level of the materials were extracted. The right panel (c) zooms in on the UPS spectra regime of the top occupied states, *i.e.* the valence band maximum. The work function of both materials was found to be 5.05 eV.

The IE comparison shows subtle changes that support the physics of the inductive effect, motivating electrochemical experiments to further explore this effect. To this aim, $Li_2Mo_4O_{13}$ was cycled in a battery *vs.* Li/Li^+ at rates of C/5 and C/10 in a voltage window between 3.5 V to 1.2 V (Figure 4). Figure 4a shows cyclic voltammetry (CV) for both $Li_2Mo_4O_{13}$ and MoO_3 at a rate of 0.1 mV sec^{-1}. The CV of $Li_2Mo_4O_{13}$ shows one main peak at 2.1 V on the first discharge, and two peaks at 2.3 V and at 2.9 V during charging. The application-relevant voltage is the delithiation (i.e. charging of half-cell) voltage. The first peak during charging represents the redox of $Mo^{6+/5+}$, and the second peak represents the redox of $Mo^{5+/4+}$. The oxidation voltage of $Mo^{6+/5+}$ in MoO_3 is measured to be 2.6 V, consistent with previous literature.[28] The $Li_2Mo_4O_{13}$ oxidation voltage is therefore 300 mV lower than the MoO_3 redox voltage vs. Li/Li^+. This oxidation in anodic voltage demonstrates that the inclusion of cations in a structure is feasible an increase by over 10% of the battery power (assuming that the total voltage is 2 V). Figure 4b presents the capacity as a function of the voltage from the second cycle to the tenth cycle. The capacity retention was found to be 78 mAh g^{-1} at a C/5 cycling rate and 82 mAh g^{-1} at a C/10 cycling rate. Although this is relatively low compared to the theoretical capacity for this material, the electrochemistry is reversible and shows minimal fade.
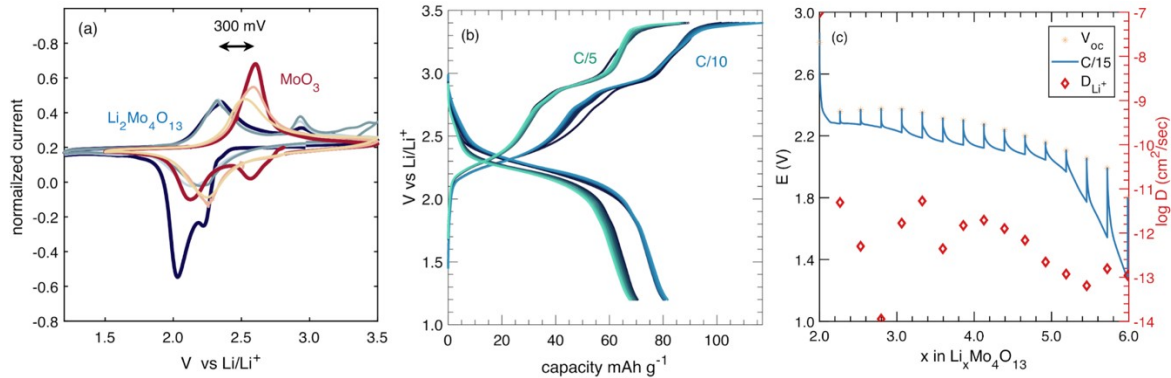
Figure 4. (a) Cyclic voltammetry of MoO_3 and $Li_2Mo_4O_{13}$ for the first three cycles. (b) Galvanostatic cycling of $Li_2Mo_4O_{13}$ at a rate of C/5 and C/10 between 1.2 V and 3.4 V, and (c) GITT measurements to calculate the Li^+ diffusion coefficient during discharge, where the yellow dots represent the open-circuit voltage ($V_{OC}(x)$) at 25 °C and the red diamonds represent the diffusion coefficient as a function of Li intercalation.

The measured capacity is equivalent to the intercalation of 2 e^- per $Li_2Mo_4O_{13}$ (0.5 Li per Mo), approximately half of the theoretical value. Low Li-ion diffusivity in the structure resulting from large particle size or irreversible electrochemical processes could contribute to this lower realized capacity. To investigate the discrepancy between the theoretical capacity and the experimental capacity, the diffusion coefficients of Li-ions were extracted from galvanostatic intermittent titration technique (GITT) measurements, based on Fick's second law.[29] The diffusion of Li during intercalation (discharge) was found to be $D_{Li+} = 10^{-12}$ -10^{-13} cm^2 sec^{-1}. This range is similar to other fast-charging anode materials, such as the Wadsley-Roth materials, and shows that Li diffusion is likely not limiting capacity retention.[30,31] To further support this claim, the measured capacity increases only slightly for slower cycling, another indication that diffusion is not the limiting parameter.

To better understand the mechanism for these electrochemical reactions, we performed *operando* XRD to provide a more detailed picture of the structural evolution of $Li_2Mo_4O_{13}$ with Li intercalation. XRD patterns were measured during the first cycle (discharge followed by charge), shown in Figure 5. The XRD patterns indicate no structural changes up to $x = 4$, where 2 additional Li are added to get a composition of $Li_4Mo_4O_{13}$. Upon further lithiation, the intensities for the peaks at 2θ = 42.5°, 25.5°, and 18.3° reduced significantly. Notably, the main peak of $Li_2Mo_4O_{13}$ at 2θ = 25.5° completely disappears. Overall, the XRD intensity is much lower after the full cycle. The changes in these diffraction patterns suggest that lithiation past $x = 4$ modify the structure. During charging (delithiation), only 2 Li-ions out of 4 Li-ions were removed. The retention of Li-ions in the structure after charging help to explain the low capacity of $Li_2Mo_4O_{13}$. Similar observations using XRD have been reported after the first lithiation for compounds such as Mo_4O_{11},[13] $Li_4Mo_5O_{17}$[26] and MoO_3[32]. While the reason for un-cyclable Li-ions in Mo-based oxides is not well understood, it is clear that the incorporation of Li electrochemically into the material can create a new, more stable phase.
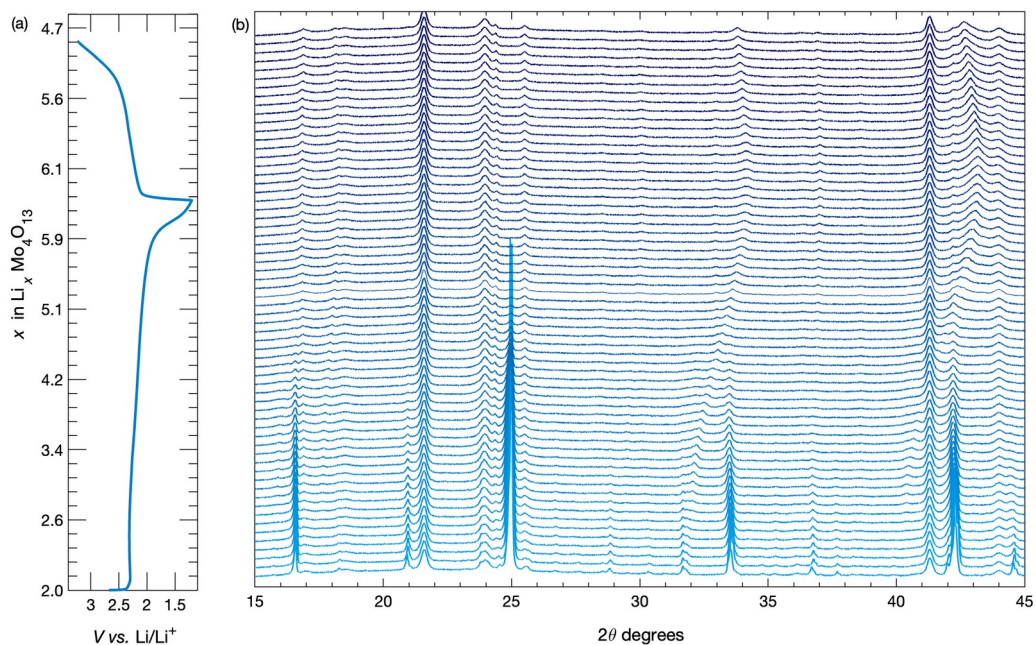
Figure 5. (a) Electrochemistry at first galvanostatic discharge/charge cycles during (b) *Operando* X-ray diffraction of $Li_2Mo_4O_{13}$. The electrochemistry shows four additional Li^+ inserted during the first discharge to form $Li_6Mo_4O_{13}$.

For clarity, the diffraction patterns of the pristine material and material after the first cycle were extracted from Figure 5b and are compared in Figure 6a. The significant discrepancy between these patterns motivate further investigation of the Mo oxidation states as a function of cycling. *Ex-situ* samples were prepared for different stages of the charge/discharge process. These samples were measured before and after the cleaning step to verify that there were no surface charging effects. Figure 5(b-d) show XPS data of a pristine, discharged (10th cycle), and charged (10th cycle) sample. The pristine sample contains only Mo^{6+}, as expected. After discharging (lithiating) $Li_2Mo_4O_{13}$, about 30% of the Mo remain as Mo^{6+} and over 50% were reduced to Mo^{5+} (Figure 6c). Charging the anode yielded a 4:6 ratio between Mo^{6+} and Mo^{5+}, as shown in Figure 6d. These data are consistent with the electrochemical results that found only two out of four Mo in the structure can reversibly host Li ions. XPS data in conjunction with the XRD data provide more insight into the structural changes, but further investigation is needed to resolve the new structure.
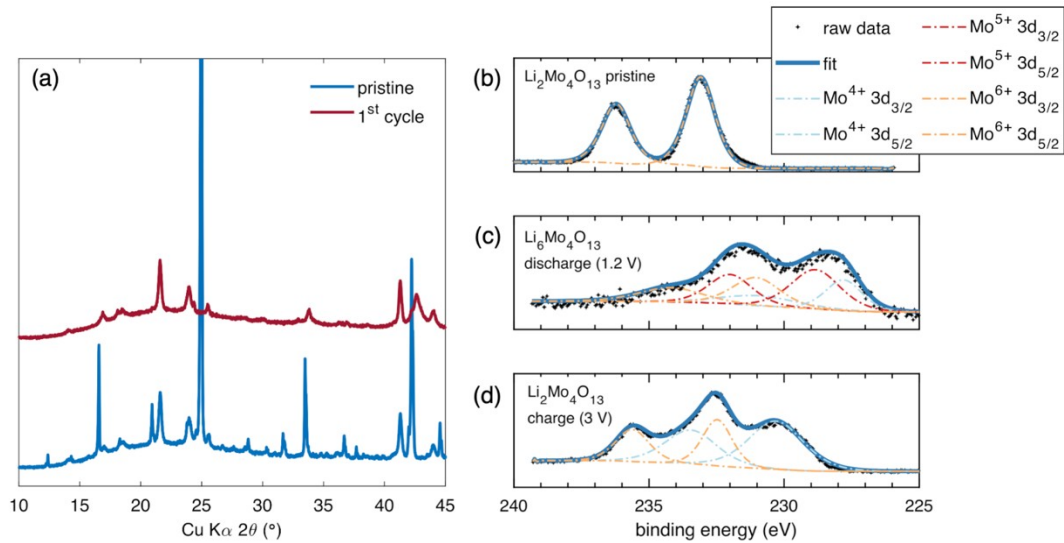
10

Figure 6. (a) XRD of the pristine material and material after the first cycle were extracted from Figure 5b and are compared. (b) X-ray photoelectron spectra displaying the Mo 3d binding energy region for pristine $Li_2Mo_4O_{13}$, (c) discharged material ($Li_6Mo_4O_{13}$), and (d) charged material. The measured data are represented by black dots and the blue line represents the total fit.

Here we present a single case study using the induction effect to lower the redox voltage using inactive cations for the molybdenum-based anode $Li_2Mo_4O_{13}$. Although they have different crystal structures, other early transition metal-based oxides, such as Nb and Ti, also show similar effects with inactive cations. Figure 7 shows the oxidation voltage of three early transition metal oxides compared with corresponding ternary compounds that contain an alkali metal. In the case of TiO_2, the voltage curves of anatase,[33] bronze,[34] and rutile[35] TiO_2 show a oxidation at 1.9 V. However, $Li_4Ti_5O_{12}$ shows redox at a lower voltage of 1.6 V.[36] The $Nb^{5+/4+}$ redox couple shows a voltage oxidation from 2 V in Nb_2O_5 to 1.9 V in $LiNb_3O_8$ when Li is added to the structure.[37,38] These examples all show that the addition of Li to a structure can reduce the redox voltage by 100 mV to 300 mV.
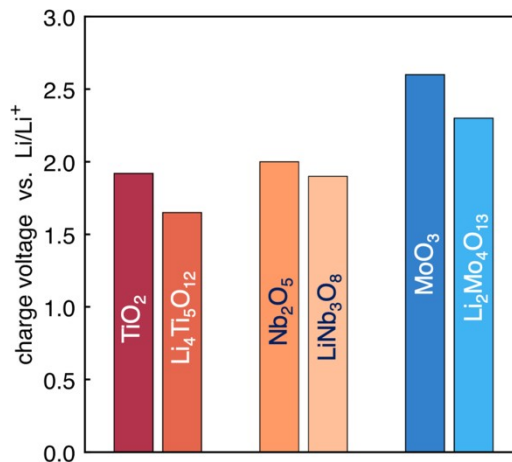

11

Figure 7: A comparison of oxidation voltages (from the peak in the CV) for three sets of d^0 transition metal oxides, with and without electropositive lithium. The data are from the following references: TiO_2,[35] $Li_4Ti_5O_{12}$,[36] Nb_2O_5,[37] and $LiNb_3O_8$.[38] Data for the Mo compounds are from this work.

To conclude, a detailed study of the ternary fully oxidized molybdenum oxide, $Li_2Mo_4O_{13}$, showed that the addition of inactive Li-ions to the structure lowers the oxidation voltage of $Mo^{6+/5+}$ by ~300 mV vs Li/Li$^+$ compared to the same redox couple in MoO_3. The additional cations increase the covalency of the M-O bonds and result in more delocalized d-electrons. UPS measurements support this hypothesis by showing a lower IE for $Li_2Mo_4O_{13}$. Both the oxidation of the voltage and the lower IE demonstrate the induction effect in this system. $Li_2Mo_4O_{13}$ shows high Li-ion diffusivity, promising for fast-charging applications. Despite somewhat lower capacity retention in $Li_2Mo_4O_{13}$, this study demonstrates the utility of the induction effect as a voltage modification strategy, pointing to alternative avenues to adjust anode voltages to maximize power density in Li-ion batteries.

Acknowledgments

References

(1) Lyu, Y.; Wu, X.; Wang, K.; Feng, Z.; Cheng, T.; Liu, Y.; Wang, M.; Chen, R.; Xu, L.; Zhou, J.; Lu, Y.; Guo, B. An Overview on the Advances of LiCoO$_2$ Cathodes for Lithium-Ion Batteries. *Adv. Energy Mater.* **2021**, *11*, 2000982.

(2) Murmann, P.; Niehoff, P.; Schmitz, R.; Nowak, S.; Gores, H.; Ignatiev, N.; Sartori, P.; Winter, M.; Schmitz, R. Investigations on the Electrochemical Performance and Thermal Stability of Two New Lithium Electrolyte Salts in Comparison to LiPF$_6$. *Electrochimica Acta* **2013**, *114*, 658–666.

(3) Hautier, G.; Jain, A.; Ong, S. P.; Kang, B.; Moore, C.; Doe, R.; Ceder, G. Phosphates as Lithium-Ion Battery Cathodes: An Evaluation Based on High-Throughput ab Initio Calculations. *Chem. Mater.* **2011**, *23*, 3495–3508.

(4) Melot, B. C.; Scanlon, D. O.; Reynaud, M.; Rousse, G.; Chotard, J.-N.; Henry, M.; Tarascon, J.-M. Chemical and Structural Indicators for Large Redox Potentials in Fe-Based Positive Electrode Materials. *ACS Appl. Mater. Interfaces* **2014**, *6*, 10832–10839.

(5) Gutierrez, A.; Benedek, N. A.; Manthiram, A. Crystal-Chemical Guide for Understanding Redox Energy Variations of $M^{2+/3+}$ Couples in Polyanion Cathodes for Lithium-Ion Batteries. *Chem. Mater.* **2013**, *25*, 4010–4016.

(6) Jung, R.; Morasch, R.; Karayaylali, P.; Phillips, K.; Maglia, F.; Stinner, C.; Shao-Horn, Y.; Gasteiger, H. A. Effect of Ambient Storage on the Degradation of Ni-Rich Positive Electrode Materials (NMC811) for Li-Ion Batteries. *J. Electrochem. Soc.* **2018**, *16*, A132–A141.

(7) Wang, C.; Appleby, A. J.; Little, F. E. Charge–Discharge Stability of Graphite Anodes for Lithium-Ion Batteries. *J. Electroanal. Chem.* **2001**, *497*, 33–46.

(8) Aurbach, D.; Zinigrad, E.; Cohen, Y.; Teller, H. A Short Review of Failure Mechanisms of Lithium Metal and Lithiated Graphite Anodes in Liquid Electrolyte Solutions. *Solid State Ion.* **2002**, *148*, 405–416.

(9) Doan-Nguyen, V. V. T.; Subrahmanyam, K. S.; Butala, M. M.; Gerbec, J. A.; Islam, S. M.; Kanipe, K. N.; Wilson, C. E.; Balasubramanian, M.; Wiaderek, K. M.; Borkiewicz, O. J.; Chapman, K. W.; Chupas, P. J.; Moskovits, M.; Dunn, B. S.; Kanatzidis, M. G.; Seshadri, R. Molybdenum Polysulfide Chalcogels as High-Capacity, Anion-Redox-Driven Electrode Materials for Li-Ion Batteries. *Chem. Mater.* **2016**, *28*, 8357–8365.

(10) Kim, H.; Lee, C.-D.; Kim, D. I.; Choi, W.; Seo, D.-H.; Yoon, W.-S. Bonding Dependent Lithium Storage Behavior of Molybdenum Oxides for Next-Generation Li-Ion Batteries. *J. Mater. Chem. A* **2022**, *10*, 7718–7727.

(11) Lee, S.-H.; Kim, Y.-H.; Deshpande, R.; Parilla, P. A.; Whitney, E.; Gillaspie, D. T.; Jones, K. M.; Mahan, A. H.; Zhang, S.; Dillon, A. C. Reversible Lithium-Ion Insertion in Molybdenum Oxide Nanoparticles. *Adv. Mater.* **2008**, *20*, 3627–3632.

(12) Yun, J.; Sagehashi, R.; Sato, Y.; Masuda, T.; Hoshino, S.; Rajendra, H. B.; Okuno, K.; Hosoe, A.; Bandarenka, A. S.; Yabuuchi, N. Nanosized and Metastable Molybdenum Oxides as Negative Electrode Materials for Durable High-Energy Aqueous Li-Ion Batteries. *Proc. Natl. Acad. Sci.* **2021**, *118*, e2024969118.

(13) Vincent, R. C.; Luo, Y.; Andrews, J. L.; Zohar, A.; Zhou, Y.; Yan, Q.; Mozur, E. M.; Preefer, M. B.; Weker, J. N.; Cheetham, A. K.; Luo, J.; Pilon, L.; Melot, B. C.; Dunn, B.; Seshadri, R. High-Rate Lithium Cycling and Structure Evolution in Mo_4O_{11}. *Chem. Mater.* **2022**, *34*, 4122–4133.

(14) Padhi, A. K.; Nanjundaswamy, K. S.; Masquelier, C.; Okada, S.; Goodenough, J. B. Effect of Structure on the Fe^{3+}/Fe^{2+} Redox Couple in Iron Phosphates. *J. Electrochem. Soc.* **1997**, *144*, 1609.

(15) Yu, K. Y.; McMenamin, J. C.; Spicer, W. E. UPS Measurements of Molecular Energy Level of Condensed Gases. *Surf. Sci.* **1975**, *50*, 149–156.

(16) Cahen, D.; Kahn, A. Electron Energetics at Surfaces and Interfaces: Concepts and Experiments. *Adv. Mater.* **2003**, *15*, 271–277.

(17) Schultz, T.; Amsalem, P.; Kotadiya, N. B.; Lenz, T.; Blom, P. W. M.; Koch, N. Importance of Substrate Work Function Homogeneity for Reliable Ionization Energy Determination by Photoelectron Spectroscopy. *Phys. Status Solidi B* **2019**, *256*, 1800299.

(18) Gatehouse, B. M.; Miskin, B. K. Structural Studies in the Li_2MoO_4-MoO_3 System: Part 1 the Low Temperature Form of Lithium Tetramolybdate, L-$Li_2Mo_4O_{13}$. *J. Solid State Chem.* **1974**, *9*, 247–254.

(19) Brower, W. S.; Parker, H. S.; Roth, R. S.; Waring, J. L. Phase Equilibrium and Crystal Growth in the System Lithium Oxide-Molybdenum Oxide. *J. Cryst. Growth* **1972**, *16*, 115–120.

(20) Gatehouse, B. M.; Miskin, B. K. Structural Studies in the Li_2MoO_4-MoO_3 System: Part 2. The High-Temperature Form of Lithium Tetramolybdate, H-$Li_2Mo_4O_{13}$. *J. Solid State Chem.* **1975**, *15*, 274–282.

(21) Verma, R.; Park, C.-J.; Kothandaraman, R.; Varadaraju, U. V. Ternary Lithium Molybdenum Oxide, $Li_2Mo_4O_{13}$: A New Potential Anode Material for High-Performance Rechargeable Lithium-Ion Batteries. *Electrochimica Acta* **2017**, *258*, 1445–1452.

(22) Wan, S.; Zhang, B.; Yao, Y.; Zheng, G.; Zhang, S.; You, J. Raman and Density Functional Theory Studies of $Li_2Mo_4O_{13}$ Structures in Crystalline and Molten States. *Inorg. Chem.* **2017**, *56*, 14129–14134.

(23) Dieterle, M.; Weinberg, G.; Mestl, G. Raman Spectroscopy of Molybdenum Oxides. *Phys. Chem. Chem. Phys.* **2002**, *4*, 812–821.

(24) Spevack, P. A.; McIntyre, N. S. A Raman and XPS Investigation of Supported Molybdenum Oxide Thin Films. 1. Calcination and Reduction Studies. *J. Phys. Chem.* **1993**, *97*, 11020–11030.

(25) Lee, S.-H.; Seong, M. J.; Tracy, C. E.; Mascarenhas, A.; Pitts, J. R.; Deb, S. K. Raman Spectroscopic Studies of Electrochromic □-MoO_3 Thin Films. *Solid State Ion.* **2002**, *147*, 129–133.

(26) Khan, R. U.; Khan, I.; Ali, B.; Muhammad, R.; Samad, A.; Shah, A.; Song, K.; Wang, D. Structural, Dielectric, Optical, and Electrochemical Performance of $Li_4Mo_5O_{17}$ for ULTCC Applications. *Mater. Res. Bull.* **2023**, *160*, 112142.

(27) Greiner, M. T.; Lu, Z.-H. Thin-Film Metal Oxides in Organic Semiconductor Devices: Their Electronic Structures, Work Functions and Interfaces. *NPG Asia Mater.* **2013**, *5*, e55–e55.

(28) Zhou, Y. Material Foundation for Future 5G Technology. *Acc Mater Res* **2021**, *2*, 306–310.

(29) Weppner, W.; Huggins, R. A. Determination of the Kinetic Parameters of Mixed‐Conducting Electrodes and Application to the System Li_3Sb. *J. Electrochem. Soc.* **1977**, *124*, 1569.

(30) Yang, Y.; Zhao, J. Wadsley–Roth Crystallographic Shear Structure Niobium-Based Oxides: Promising Anode Materials for High-Safety Lithium-Ion Batteries. *Adv. Sci.* **2021**, *8*, 2004855.

(31) Tanibata, N.; Kato, M.; Takimoto, S.; Takeda, H.; Nakayama, M.; Sumi, H. High Formability and Fast Lithium Diffusivity in Metastable Spinel Chloride for Rechargeable All-Solid-State Lithium-Ion Batteries. *Adv. Energy Sustain. Res.* **2020**, *1* (1), 2000025.

(32) Tsumura, T.; Inagaki, M. Lithium Insertion/Extraction Reaction on Crystalline MoO_3. *Solid State Ion.* **1997**, *104*, 183–189.

(33) Xu, J.; Jia, C.; Cao, B.; Zhang, W. F. Electrochemical Properties of Anatase TiO2 Nanotubes as an Anode Material for Lithium-Ion Batteries. *Electrochimica Acta* **2007**, *52*, 8044–8047.

(34) Liang, S.; Wang, X.; Qi, R.; Cheng, Y.-J.; Xia, Y.; Müller-Buschbaum, P.; Hu, X. Bronze-Phase TiO2 as Anode Materials in Lithium and Sodium-Ion Batteries. *Adv. Funct. Mater.* **2022**, *3*, 2201675.

(35) McNulty, D.; Carroll, E.; O'Dwyer, C. Rutile TiO2 Inverse Opal Anodes for Li-Ion Batteries with Long Cycle Life, High-Rate Capability, and High Structural Stability. *Adv. Energy Mater.* **2017**, *7*, 1602291.

(36) Yuan, T.; Tan, Z.; Ma, C.; Yang, J.; Ma, Z.-F.; Zheng, S. Challenges of Spinel $Li_4Ti_5O_{12}$ for Lithium-Ion Battery Industrial Applications. *Adv. Energy Mater.* **2017**, *7*, 1601625.

(37) Liu, M.; Yan, C.; Zhang, Y. Fabrication of Nb_2O_5 Nanosheets for High-Rate Lithium Ion Storage Applications. Sci. Rep. 2015, 5, 8326.

(38) Jian, Z.; Lu, X.; Fang, Z.; Hu, Y.-S.; Zhou, J.; Chen, W.; Chen, L. $LiNb_3O_8$ as a Novel Anode Material for Lithium-Ion Batteries. *Electrochem. Commun.* **2011**, *13*, 1127–1130.